

Interpretable representation learning of quantum data enabled by probabilistic variational autoencoders

Paulin de Schoulepnikoff, Gorka Muñoz-Gil,^{*} Hendrik Poulsen Nautrup, and Hans J. Briegel
University of Innsbruck, Department for Theoretical Physics, Technikerstr. 21a, A-6020 Innsbruck, Austria
 (Dated: June 19, 2025)

Interpretable machine learning is rapidly becoming a crucial tool for scientific discovery. Among existing approaches, variational autoencoders (VAEs) have shown promise in extracting the hidden physical features of some input data, with no supervision nor prior knowledge of the system at study. Yet, the ability of VAEs to create meaningful, interpretable representations relies on their accurate approximation of the underlying probability distribution of their input. When dealing with quantum data, VAEs must hence account for its intrinsic randomness and complex correlations. While VAEs have been previously applied to quantum data, they have often neglected its probabilistic nature, hindering the extraction of meaningful physical descriptors. Here, we demonstrate that two key modifications enable VAEs to learn physically meaningful latent representations: a decoder capable of faithfully reproducing the probability distributions of quantum states and a probabilistic loss tailored to this task. Using benchmark quantum spin models, we identify regimes where standard methods fail while the representations learned by our approach remain meaningful and interpretable. Applied to experimental data from Rydberg atom arrays, the model autonomously uncovers the phase structure without access to prior labels, Hamiltonian details, or knowledge of relevant order parameters, highlighting its potential as an unsupervised and interpretable tool for the study of quantum systems.

I. INTRODUCTION

The rapid progress of classical machine learning (ML) is profoundly impacting our ability to analyze quantum systems and process quantum data, paving the way for new paradigms in scientific discovery [1]. In the quantum domain, by leveraging both supervised and unsupervised learning methods, researchers are now able to identify quantum phase transitions [2–4], model complex entanglement features [5], and improve quantum state tomography [6]. Notably, neural networks have been shown to offer compact and expressive representations of quantum states, capable of capturing their intricate correlations and phase structure [7].

Beyond its predictive capacity, ML techniques with enhanced interpretability can serve as a lens through which the intrinsic properties of quantum systems can be unravelled [8]. For example, support vector machines have been employed to identify order parameters [9], symbolic regression methods have revealed underlying equations of motion [10], and neural architectures leveraging correlation functions have been used to map out phase diagrams of experimental quantum many-body systems [11]. Among these interpretable models, variational autoencoders (VAEs) [12] have attracted attention due to their ability to autonomously extract meaningful and minimal representations of some input dataset in their *latent space* [13]. When applied to physics datasets, this relates to extracting the meaningful physical features of the system of study [1]. In the quantum realm, VAEs have been used for instance to study phase transitions in spin systems [14, 15].

Nonetheless, one of the key challenges when applying machine learning methods to quantum data lies in its intrinsically stochastic nature. As a result, physical observables must be inferred statistically over repeated measurements. This is particularly challenging in experimental platforms such as ultra-cold atoms in optical lattices [16] or trapped-ion quantum simulators [17], where performing repetitive measurement is costly, often leading to poor statistics. This fundamental stochasticity has motivated the development of ML approaches that operate directly on individual measurement outcomes, bypassing the need for full state reconstruction and instead learning meaningful features from single or ensembles of quantum snapshots [3, 4, 18, 19].

In this sense, accounting for the intrinsic stochasticity of quantum data is essential for developing interpretable machine learning models. Since the physical properties of a quantum system are fundamentally encoded in its probability distribution, capturing this distribution is necessary for any meaningful characterization. This is particularly critical for VAEs: if they cannot reproduce the properties of the underlying probabilistic distribution of its input, it will not be able to create meaningful representations in its latent space. However, existing VAE applications on quantum data have not considered this stochasticity [14, 15, 20–22]. In particular, they commonly use of deterministic losses, which fundamentally misaligns with the goal of learning the probability distribution of the target quantum states. Such losses direct the model to capture only one-body, or *mean-field*, features, thereby neglecting nontrivial many-body correlations. It is hence critical to develop architectures that can cope with the stochastic properties of the quantum data, if one aims to use this method to extract physical features.

To tackle these challenges, we propose two key adap-

^{*} gorka.munoz-gil@uibk.ac.at

tions to the VAE architecture. First, we train the model to directly approximate the underlying probability distribution of the input data, rather than exactly reconstructing particular samples. Second, we adapt the VAE's decoder to be able to capture the stochastic properties of effectively any target quantum state. To achieve the latter, we draw inspiration from Neural Quantum States (NQS) [7], neural network architectures used as expressive variational ansätze capable of representing quantum probability distributions.

To demonstrate the impact of the proposed improvements into the VAE framework for quantum data, we compare its resulting performance to that of a standard deterministic VAE on two paradigmatic spin models: the transverse-field Ising model with next-nearest neighbour interactions (NNN-TFIM) and long-range interactions (LR-TFIM). Through these models, we will explore and identify regimes where conventional VAEs struggle while the presented method provides physically interpretable representations. We further validate the approach on experimental snapshots of Rydberg atom arrays [16]. Without access to any prior labeling, knowledge of the governing Hamiltonian nor the number of relevant order parameters, the model is able to autonomously uncover the underlying phase structure, underscoring its potential as a powerful unsupervised and interpretable tool for the study of quantum many-body systems.

II. METHODS

In this section we provide a detailed introduction to variational autoencoders (VAEs), outlining their fundamental principles. We then introduce the key adaptations required to effectively handle the stochastic nature of quantum data.

A. Background on Variational Autoencoders

Variational Autoencoders (VAEs) consist of three main components: an encoder, a latent space, and a decoder [12]. The encoder compresses the input data into a lower-dimensional representation, namely the latent space. In contrast to autoencoders, the latent space of VAEs is parameterized by a probability distribution, typically defined as a multivariate Gaussian distribution. In practice, the encoder outputs the mean μ_i and variance σ_i of the latent variables from which the values for each latent neuron z_i are sampled and subsequently passed to the decoder (see Fig. 1). The decoder then reconstructs the input data based on the sampled latent variables.

The objective of Variational Autoencoders is to approximate an unknown probability distribution $p(x)$, assumed to underlie a given dataset. Directly computing this likelihood is generally intractable for high-dimensional data, so VAEs optimize a tractable lower bound known as the Evidence Lower Bound (ELBO). From the previous, the

loss with which the model is then trained can be written as

$$\mathcal{L} = \frac{1}{N} \sum_{n=1}^N \mathbb{E}_q[\log p(x^{(n)}|z)] - \beta \text{KL}[q(z|x^{(n)})||p(z)] \quad (1)$$

with N being the number of samples $x^{(n)}$ in the training set.

The loss function introduced in Eq. (1) contains two terms. First, a reconstruction loss, which enforces similarity between the input and output data. Second, a regularization term, which minimizes the Kullback-Leibler (KL) divergence between the latent space distribution $q(z_i) \sim \mathcal{N}(\mu_i, \sigma_i)$ and the prior $p(z)$, typically defined as standard normal distribution $p(z) \sim \mathcal{N}(0, 1)$. This term acts as a regularizer, enforcing the latent representation to align with the prior distribution. However, if all latent variables were to collapse to the prior, the decoder would lack sufficient information to faithfully reconstruct the data, leading to an increase in the reconstruction loss. This trade-off induces a natural competition between the two terms in the loss function, such that only the minimal set of latent neurons needed to properly reconstruct the input diverge from the prior (commonly referred to as an *active* neuron), while the other neurons are "noised out" and collapse to $p(z)$ (referred to as *passive* neurons). Moreover, one can further scale the regularization term with a hyperparameter β [13], such that the two terms are properly balanced. In practice, this mechanism forces the model to retain only the essential information from the input data in the latent space. When such data is associated with a few hidden variables, e.g. the degrees of freedom of a physical system, the resulting latent representation tends to align with these [1, 23, 24].

B. VAE with a generative decoder

As discussed in the introduction, prior applications of VAEs to quantum data have largely employed architectures with deterministic decoders [14, 15, 20–22]. In these models, the decoder is trained to reconstruct individual spin configurations using a deterministic reconstruction loss between input and output spin configurations, as for instance the mean squared error (MSE). This approach implicitly assumes a deterministic relationship between the latent representation and the output configuration, neglecting the intrinsic probabilistic nature of quantum measurement outcomes. Moreover, the use of a deterministic reconstruction metric enforces the model to learn average configurations across samples rather than capturing the full probability distribution of outcomes. This leads to a latent space that reflects only the mean-field structure of the data, failing to capture any probabilistic feature, as for instance correlations between nearby spins. In what follows, we refer to this baseline model as the *deterministic* VAE (dVAE) to distinguish it from the stochastic decoder architecture introduced in this work.

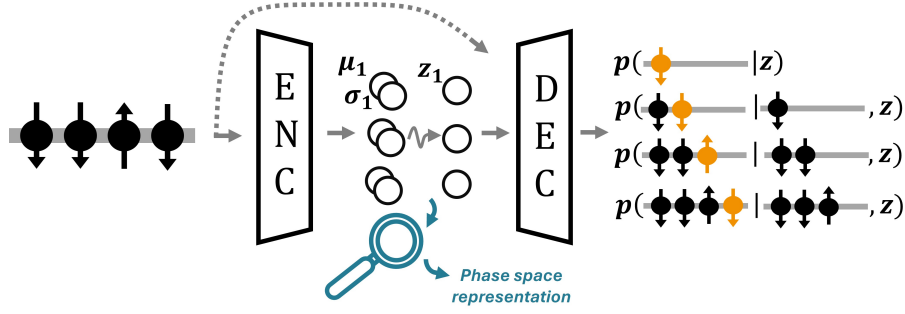


FIG. 1. **Schematic representation of the cpVAE.** A spin configuration is input into the encoder neural network ENC. The latter outputs the means μ_i and the variances σ_i parameterizing the Gaussian distribution from which the latent variables z_i are sampled. Then, the decoder neural network DEC takes as input the latent variables and outputs the conditional probabilities of each spin be in a given state (up or down in the present scheme). During training, the decoder also receives as input the spin configuration to be reconstructed by the conditional probabilities, as indicated with the dotted arrow. Once trained, the latent neurons z_i encode the main physical features of the physical system, which directly relate to its phase space. Moreover, one can fix the value of the latent variables and generate new configurations by autoregressively sampling the output conditional probabilities.

Motivated by the recent work on VAEs for stochastic processes [24] and arguments on using generative classifiers for phase-classification [25], we present here the key changes that will allow VAE to correctly create interpretable representations of quantum data. First, we construct a decoder inspired by the recent advances in Neural Quantum States (NQS) [26]. For example, NQS have recently demonstrated impressive performance in ground-state searches and non-equilibrium dynamics [27]. By integrating an NQS-based decoder into the VAE framework, we ensure that the model can accurately capture and regenerate the statistical structure of the input quantum states.

Second, we propose replacing the deterministic loss with a probabilistic reconstruction loss. Rather than attempting to reproduce individual measurement outcomes, which is fundamentally intractable due to the inherent stochasticity of quantum systems, we instead train the model to learn the underlying probability distribution from which these input samples are drawn. Indeed, when dealing with a quantum system, a single measurement outcome cannot be used to fully characterize it. Instead, one needs to model the full distribution over all possible outcomes. By aligning the decoder's objective with this principle, the model becomes capable of capturing the essential statistical structure of the quantum state, rather than averaging over its fluctuations.

To account for the two previous arguments, we propose the use of an auto-regressive neural network (ARNN) for the decoder (see Fig. 1 and Appendix A for further details), and train it to model the conditional probabilities of each spin configuration, given the preceding spins. More precisely, the configuration of spin i is given by the Bernoulli distribution. Its probability mass function f over the two possible outcomes $x_i \in 1, -1$ is

$$f(p_i, x_i) = p_i^{x_i-1} (1 - p_i)^{x_i+1}, \quad (2)$$

with p_i being predicted by the decoder. Without loss of

generality, the whole spin configuration is written as the product of the conditional probabilities of each spin,

$$p(x) = \prod_{i=1}^N p(x_i | x_0, x_1, \dots, x_{i-1}). \quad (3)$$

Hence, each output of the decoder models a conditional probability

$$p_i := p(x_i | x_0, x_1, \dots, x_{i-1}). \quad (4)$$

We will refer to this model as cpVAE, standing for *conditional probabilistic* VAE. Given these considerations, the reconstruction loss (first term in Eq. (1)) can be rewritten as

$$\begin{aligned} \mathbb{E}_{z \sim q} [\log p(x_n | z)] &= \mathbb{E}_{z \sim q} \sum_i (x_i - 1) \log p_i \\ &\quad + (x_i + 1) \log(1 - p_i). \end{aligned} \quad (5)$$

To compute the KL regularization (second term in Eq. (1)), we adopt the decomposition introduced in the Total Correlation Variational Autoencoder (TC-VAE) framework [28]. This approach enables a fine control over the structure of the latent space, by explicitly penalizing statistical dependencies between latent variables. This enforces the distinct degrees of freedom of some input physical data to be stored in independent latent neurons. The ELBO TC-decomposition consists in rewriting the KL regularization as

$$\begin{aligned} \mathbb{E}_{p(x)} [\text{KL}(q(z|x) || p(z))] &= \text{KL}(q(z, x) || q(z)q(x)) \\ &\quad + \text{KL}(q(z) || \prod_j q(z_j)) \\ &\quad + \sum_j \text{KL}(q(z_j) || p(z_j)). \end{aligned} \quad (6)$$

In the latter, the first term on the right-hand side is the mutual information $I_q(z; x)$. The second term, referred

to as the total correlation (TC), encourages the model to learn as so-called disentangled representations [28], where individual latent units capture distinct, minimally correlated physical features of the data. The third term is the dimension-wise KL which aligns the latent variables with the prior $\mathcal{N}(0, 1)$. The hyperparameters, α , β and γ are introduced to control the weight of each of these terms. The full loss with which the model is trained is thus

$$\begin{aligned} \mathcal{L} = & \mathbb{E}_{z \sim q} \sum_i (x_i - 1) \log p_i + (x_i + 1) \log(1 - p_i) \\ & - \alpha I_q(z; n) - \beta \text{KL}(q(z) \| \prod_j q(z_j)) \\ & - \gamma \sum_j \text{KL}(q(z_j) \| p(z_j)). \end{aligned} \quad (7)$$

III. RESULTS

To assess the performance of the proposed cpVAE architecture, we begin by benchmarking its performance against a dVAE on two well-established quantum spin models. These controlled settings will allow us to identify the limitations of deterministic decoders, as for instance their inability to capture non-trivial features beyond the mean-field behavior. They will also demonstrate that the proposed probabilistic approach yields representations that more accurately reflect the underlying physics.

The first spin model is the transverse-field Ising model (TFIM) with next-nearest-neighbor (NNN) interaction. For weak NNN coupling, the model effectively reduces to the conventional TFIM, a setting where prior studies have applied deterministic VAEs [14, 20, 21]. In this regime, we show that this success is largely due to the fact that the relevant order parameter is a mean-field observable. As the strength of the NNN interaction increases, the system deviates from such mean-field behavior, and we observe that the deterministic VAE fails to reconstruct physical features, in contrast to the probabilistic one, effectively hindering the representation of the system in their latent space.

We further compare both models on the TFIM with long-range interactions (LR-TFIM), where the interplay between quantum fluctuations and non-local couplings poses an additional challenge. In this setting, we show that a probabilistic variant of VAE is essential for capturing the relevant physical features in the latent space.

Finally, we apply our architecture to experimental data obtained from Rydberg atom arrays. Despite the complexity and stochastic nature of the measurements, we will show that the model autonomously uncovers meaningful latent representations that reflect the phase structure of the system, without any supervision or prior knowledge of the underlying Hamiltonian.

The code needed to reproduce the results presented in each figure is available in the accompanying code repository [29].

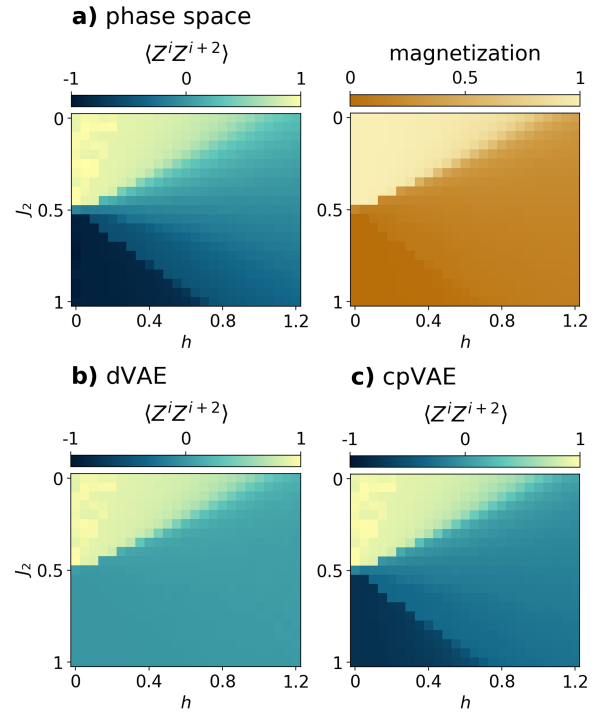


FIG. 2. **Next-nearest-neighbor transverse-field Ising model.** **a)** Next-nearest-neighbor correlator (left) and magnetization (right) computed from training set configurations across the phase space. **(b,c)** Next-nearest-neighbor correlator of the generated spin configurations across the phase space generated by the dVAE and cpVAE, respectively.

A. Spin Models

1. NNN-TFIM

We start by considering the Transverse Field Ising Model with nearest neighbour and next-nearest-neighbour interaction (NNN-TFIM) in a one dimensional chain, whose Hamiltonian has the form[30]

$$H_{NNN-TFIM} = \sum_{i=1}^N -Z^i Z^{i+1} + J_2 Z^i Z^{i+2} + h X^i, \quad (8)$$

with $J_2 \in [0, 1]$ and X^i, Z^i being the Pauli's operators on spin i . The system under consideration has a size of $N = 20$ with periodic boundary conditions.

The phase diagram of the NNN-TFIM can be characterized using two observables: the next-nearest-neighbor correlator $\langle Z^i Z^{i+2} \rangle$ and the magnetization $\langle Z^i \rangle$, as shown in Fig. 2a. For coupling strengths $J_2 < 0.5$, the nearest-neighbor interaction dominates, and the system effectively reduces to the conventional TFIM, a regime where deterministic VAEs had previous success [14, 20, 21].

As J_2 increases, the next-nearest-neighbor antiferromagnetic interaction becomes dominant. Due to the one-dimensional topology of the lattice, this term induces a geometric frustration. In particular, for $J_2 > 0.5$ and

small transverse field h , the system enters an antiferromagnetic phase characterized by alternating strong and weak nearest-neighbor correlations.

We then train the cpVAE with configurations arising from different points in the phase space of this spin model. During training, we see that a single neuron remains active, while all other neurons collapse to the prior and are noise out (see Appendix B for further details). This is to be expected since, as shown in Fig. 2a, the whole phase space can be characterized only by the second nearest-neighbour correlator. To mitigate the effect of hyperparameter tuning and to make the comparison as fair as possible, we then train the dVAE without KL regularization and with a latent dimension of 1. We note that not doing so, and considering a larger latent space, would allow the dVAE to store some stochastic features of the input sample in the latent space, for example, particular spins being up or down.

Reconstruction analysis We then benchmark the generative capabilities of both models. To do so, we first input configurations from the whole phase space to the encoder, extract the corresponding latent space, and then sample new configurations from the decoder based on the extracted latent variables. In Fig. 2(b), we show the $\langle Z^i Z^{i+2} \rangle$ correlator for the output configurations of the dVAE across the phase. While the model accurately reproduces the expected correlations in both the ferromagnetic and paramagnetic regimes, it fails to capture the antiferromagnetic phase. Importantly, this regime cannot be characterized by the magnetization only, the usual order parameter extracted in previous works. Since the alternating bond structure inherent to the frustrated ground state falls beyond any mean-field parameter, the deterministic decoder is unable to correctly reproduce these statistics, and hence the antiferromagnetic phase will never appear in the latent representation of a dVAE.

In contrast, we show in Fig. 2c that the cpVAE is able to accurately reproduce the desired statistics across the full phase space, including the antiferromagnetic region. Notably, this accuracy is maintained even when the model is trained on a restricted subset of the parameter space (see Appendix C), demonstrating its capacity to generalize beyond the training domain. This highlights the ability of the cpVAE to capture many-body correlations that elude deterministic approaches, reinforcing the importance of a probabilistic generative model when learning from intrinsically stochastic quantum data.

2. LR-TFIM

As a second benchmark, we consider the long-range transverse field Ising model (LR-TFIM), which has been recently performed experimentally via trapped-ion simulators [17, 31, 32]. This model is a modification of the conventional TFIM in which spin-spin interactions decay

algebraically with distance. Its Hamiltonian is given by

$$H_{LR-TFIM} = \sum_{i=1}^N hX^i - \sum_{j \neq i} \frac{Z^i Z^j}{|i-j|^\alpha}, \quad (9)$$

where α controls the range of the interactions: smaller values of α correspond to a slower decay and hence longer-range couplings. To better reflect typical experimental conditions, we simulate the system using open boundary conditions. A chain of $N = 20$ spins is considered.

At small transverse field strengths h , the ground state is ferromagnetic, with all spins aligned in the same direction. For large h , the spins are aligned in the direction of the transverse field, leading to a paramagnetic phase. The ground state becomes then a product state devoid of long-range correlations. These two phases can be clearly visually differentiated by means of the total magnetization, as we show in Fig. 3a. Moreover, for intermediate values, the system exhibits quantum fluctuations with nontrivial many-body entanglement and algebraically decaying spin-spin correlations. The latter can be expressed as

$$C(r) = \langle Z^i Z^{i+r} \rangle \sim \frac{1}{r^{\beta(\alpha, h)}}, \quad (10)$$

where the exponent β is an indicator of the correlation strength and spread.

Training the cpVAE on configurations arising from this spin model, we observe that two latent neurons survive (see Appendix B). As in the previous section, the dVAE was trained without KL regularization and imposing the same latent dimension found with the cpVAE.

Latent space analysis In this case, rather than focusing on the output of the models, we will directly analyze their latent space, to better understand the representations learned by the two variants. To do so, we input configurations sampled at different points of the phase space and analyze the mean value of the two surviving neurons μ_i output by the encoder.

The latent space learned by the deterministic VAE (dVAE) is shown in Fig. 3b. Due to the inability of the decoder to properly account for the correlations of the model, the latent neurons of dVAE follow the same behavior as the total magnetization. Indeed, both neurons exhibit similar behavior, effectively collapsing onto a representation that distinguishes only the ferromagnetic phase. As a result, the dVAE fails to capture any meaningful structure beyond mean-field characteristics, such as those arising in the critical or intermediate regimes.

In contrast, the latent space learned by the cpVAE (Fig. 3c) exhibits a markedly richer structure. The first latent neuron, μ_1 , correlates strongly with a magnetization-like observable (see Appendix D for more details), which is consistent with it capturing the dominant factor of variation in the data. The second, μ_2 , encodes a distinct feature that highlights the presence of an intermediate phase emerging at low values of α and h . To investigate

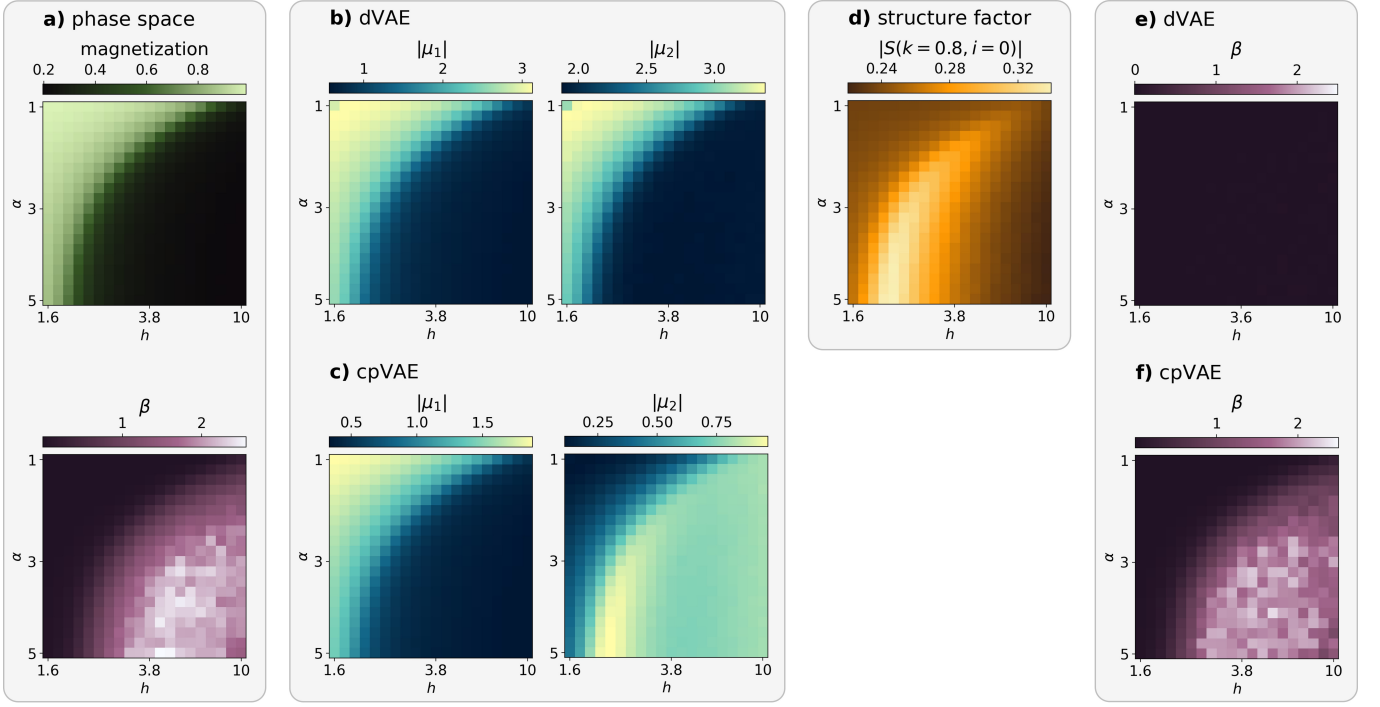


FIG. 3. **LR-TFIM.** **a)** Magnetization (top) and β exponent from Eq. (10) (bottom) computed from training set configurations across the phase space. **(b,c)** Absolute value of the learned latent space mean values μ_i for the two active neurons, for the dVAE and cpVAE, respectively, and for input configurations across the phase space. **d)** Structure factor from Eq. (11) with $k = 0.8$ and $i = 0$ for training set configurations across the phase space. **(e,f)** β exponent for spin configurations generated by the dVAE and the cpVAE, respectively. The former has values $\beta = 0$ for across the whole phase space.

this further, we applied symbolic regression [33] to the latent values of μ_2 , seeking a compact analytical expression $f(x)$ that best describes its behavior given the corresponding spin configuration x . This approach suggests that the neuron was encoding a quantity similar to the structure factor [34]

$$S(k, i) = \frac{1}{N} \sum_j e^{2\pi k |j-i|/N} \langle Z^j Z^i \rangle. \quad (11)$$

As shown in Fig. 3(d), the structure factor, evaluated here at fixed momentum $k = 0.8$ and spatial reference site $i = 0$, highlights the same region of the phase diagram as captured by the latent variable μ_2 . From a physical perspective, the structure factor reveals a distinct intermediate regime between the ferromagnetic phase and the high β paramagnetic regime. This feature, visible only at the chain boundaries (i.e., $i = 0$ and $i = N$), suggests the emergence of a boundary-induced phase, likely arising from finite-size and open-boundary effects [35]. That the cpVAE identifies this behaviour without supervision underscores its potential as a tool for uncovering non-trivial structure in many-body systems and guiding the formulation of new hypotheses.

Reconstruction analysis To further demonstrate the importance of the probabilistic decoder, we now perform the same analysis on generated configurations as done in the previous section. We then compute the correlation

exponent β from Eq. (10). As expected, the dVAE fails to reproduce the spatial correlations present in the data, yielding spin configurations with $\beta = 0$ across the entire phase space, hence without the expected polynomial decay. In contrast, the cpVAE correctly recovers the spatial structure of the quantum states. The reconstructed configurations exhibit β exponents in quantitative agreement with the ground-state correlations across the entire phase space. This result confirms that the cpVAE not only correctly captures mean-field features such as magnetization but also encodes nontrivial many-body correlations.

B. Experimental Rydberg Atoms

As a final benchmark, we train the cpVAE with experimental snapshots obtained from a programmable Rydberg atom array [16]. The setup consists of a two-dimensional square lattice with $N = L \times L$ atoms, where each atom resides in either its electronic ground state $|g\rangle$ or an excited Rydberg state $|r\rangle$. The latter is achieved via laser-driven excitation of an outer electron to a high-lying energy level, giving rise to strong, long-range interactions between excited atoms. This platform provides an ideal testbed for the cpVAE, as it exhibits a variety of quantum phenomena, including frustration, quantum criticality and emergent spatial order, all encoded in the projective measurement snapshots. Our aim here is to assess whether cpVAE

can extract meaningful latent representations from such data, despite the presence of experimental noise and the stochastic nature of quantum measurement.

The Rydberg array under study is characterized by the Hamiltonian

$$H_{\text{Rydberg}} = \sum_{i < j} \frac{C_6}{\|\mathbf{r}_i - \mathbf{r}_j\|^6} \hat{n}_i \hat{n}_j - \Delta \sum_i \hat{n}_i - \frac{\Omega}{2} \sum_i \sigma_i^x \quad (12)$$

with

$$\hat{n}_i = \frac{1}{2}(\sigma_i^z + \mathcal{I}) \quad \text{and} \quad C_6 = \Omega \left(\frac{R_b}{a} \right)^6, \quad (13)$$

where $\sigma_i^x = |g\rangle_i \langle r|_i + |r\rangle_i \langle g|_i$, $\sigma_i^z = |r\rangle_i \langle r|_i - |g\rangle_i \langle g|_i$, Δ is the detuning from resonance, Ω the Rabi frequency, a the lattice length scale and R_b the Rydberg blockade radius. A key feature of Rydberg atoms is that, when a given atom is in the excited state $|r\rangle$, the van der Waals potential effectively prevents the excitation of any other atom within a radius R_b , an effect commonly referred to as the "Rydberg blockade" [36, 37]. The experimental setup considered here, consisting of an array of 13×13 atoms, allows for the tuning of two different parameters: R_b/a , controlling the strength of the blockade, and Δ/Ω encoding the relative strength of a longitudinal field. To create the snapshots, the neutral atoms went through a coherent quantum evolution for different values of blockade strength R_b/a and relative field strength Δ/Ω . Then, a projective readout is performed in order to determine which atoms were not in the excited Rydberg state $|r\rangle$ [4, 16].

The phase space of the described system is illustrated in Fig. 4a. First, three different phases, namely the checkerboard, star and striated phases can be identified through the different Fourier-space order parameters [16]

$$\tilde{\mathcal{F}}(k_1, k_2) = \langle \mathcal{F}(k_1, k_2) + \mathcal{F}(k_2, k_1) \rangle / 2 \quad (14)$$

with

$$\mathcal{F}(\mathbf{k}) = \left| \frac{1}{\sqrt{N}} \sum_i e^{i\mathbf{k} \cdot \mathbf{x}_i / a} n_i \right|. \quad (15)$$

Each panel in Fig. 4a shows the particular parameter used to identify each phase (see panels' titles), with insets showcasing exemplary configurations of each phase on a smaller 9×9 lattice. Moreover, an edge-ordered phase can be also recognized by the difference between the nearest neighbour correlator of atoms at the edge and at the bulk of the array. For $R_b/a > 1.5$ and between the edge-ordered and the star phase, an additional ordered phase was identified in Ref. [4].

We train the cpVAE on experimental snapshots collected across a range of control parameters R_b/a and Δ/Ω (see details in Appendix B). We observe for this dataset

that only two latent neurons remain active. Their behaviour across the phase diagram is presented in Fig. 4b, where we plot their mean μ_i , absolute means $|\mu_i|$ and variances σ_i (see Fig. 1).

The left columns, corresponding to μ_i , reveal that the latent dimensions are sufficient to discriminate between distinct quantum phases. For example, the regime in which the system energetically favors minimizing the number of atoms in the $|r\rangle$ state ($\Delta/\Omega < 0$) is characterized by low μ_1 and high μ_2 values. Then, the star phase shows low values of μ_1 , the striated phase low values in both components, and the checkerboard phase exhibits large μ_1 . By analyzing the absolute values $|\mu_i|$ (central columns of Fig. 4b), we found an even better resolved picture of the latent space, where the boundary-ordered phase is clearly highlighted for $|\mu_1| = 0$.

The right columns of Fig. 4b display the variances σ_i of the latent dimensions, which quantify the uncertainty associated with each neuron's encoding. Lower values of σ_i correspond to narrower posterior distributions, implying reduced variability in the sampled latent variable z_i around its mean μ_i . While the KL regularization term in the loss function encourages larger σ_i to match the unit-variance prior $p(z)$, this pressure is counteracted by the reconstruction loss, which favours more precise sampling. In regions of the phase diagram where redundant or non-discriminative information is encoded, the model can tolerate increased variance without compromising reconstruction accuracy. This effect is visible, for example, at $\Delta/\Omega < 0$, corresponding to nearly no atoms in the $|r\rangle$ state, where σ_i becomes large. By inspecting the variance across the latent dimensions, one gains insight into their relative importance in different regions of the latent space. In particular, the first latent shows reduced variance in the vicinity of the boundary-ordered and checkerboard phases, indicating its relevance in encoding these features. Conversely, the second latent exhibits small variance around the star and striated phases, suggesting its role in resolving these configurations. A similar study of the variances of the cpVAE trained on the spin model is provided in Appendix E, where we also further analyze their relationship to the informational content of the input configuration.

We emphasize that the cpVAE operates entirely unsupervised and does not rely on any prior knowledge of the system's Hamiltonian, symmetries, or phase boundaries. Despite this, it captures nontrivial structure in the data, organizing the snapshots into a meaningful latent geometry that, surprisingly, qualitatively matches the underlying phase diagram of the system. This demonstrates the power of probabilistic generative models to autonomously extract interpretable features from experimental quantum systems.

IV. DISCUSSION

In this work, we have presented a series of modifications on the VAE architecture essential to create interpretable

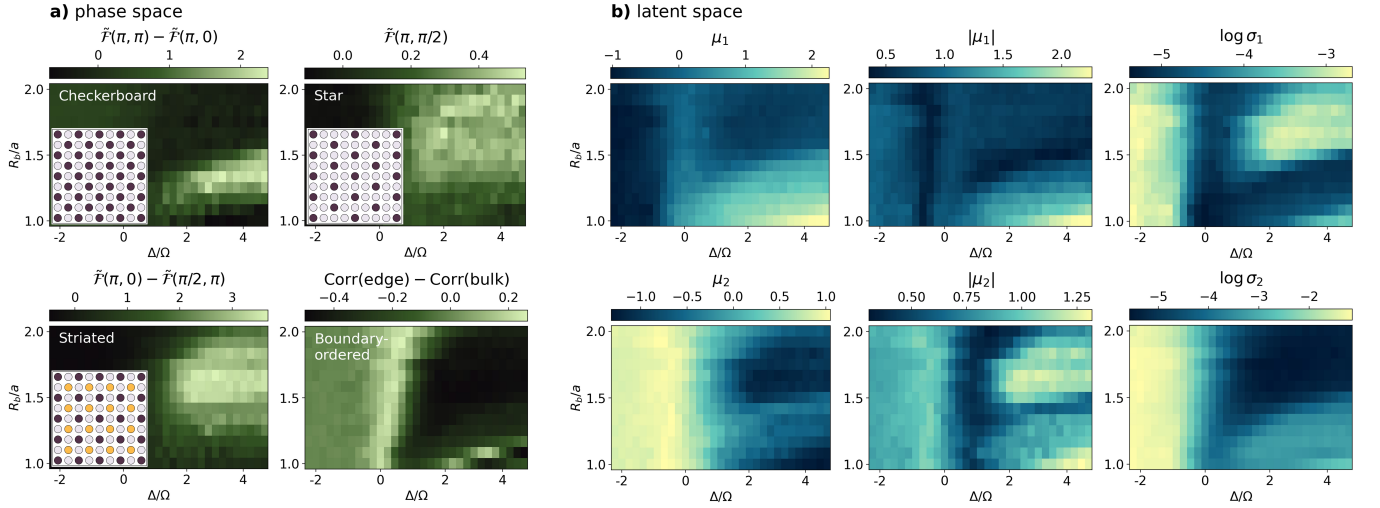


FIG. 4. **Experimental Rydberg atoms array.** **a)** Different Fourier-space order parameters (Eq. (15)) highlighting the location of the checkerboard, star and striated phases across the phase space. The boundary ordered phase is located by means of the difference between the nearest-neighbor correlator for atoms at the edge and the bulk of the array. The insets showcase exemplary configurations of each phase on a smaller 9×9 lattice, with white, purple and orange circles representing atoms in the $|g\rangle$, $|r\rangle$ and $|+x\rangle$ states, respectively. **b)** Latent representation learned by the cpVAE. For the two remaining active neurons, we present here the mean values (left) and variances (right) as output by the encoder, for input configurations across the phase space. We also show the absolute mean values (center), which showcase a finer resolution of the learned latent space.

representations of quantum data. We have shown that two key aspects are crucial for this. First, as quantum data is intrinsically random, deterministic losses such as the mean square error will fail to capture the properties of most quantum systems. Instead, following common approaches in ML generative modeling, one rather needs to train the VAE to approximate the underlying probability distribution of the input data. Second, and closely related to the previous statement, the generative model must be able to generate data with same statistical properties as the input one. To this aim, we took inspiration from the recent advancements on neural quantum states (NQS), creating the VAE’s decoder aligned with these architectures, ensuring that it can correctly reconstruct the quantum states under study.

By training different variants of VAEs in two paradigmatic spin models, we showed that failing to account for the intrinsic stochasticity of quantum data fundamentally limits the capacity of VAE to capture features beyond mean-field descriptors. In contrast, considering the aforementioned improvements enables the reconstruction of nontrivial correlation patterns and results in a latent space representation that matches the underlying structure of the quantum data. We then used such architecture to explore the phase space of snapshots obtain in an experimental setup of Rydberg atom arrays, demonstrating the ability of the model to uncover the structure of the underlying phase space and to distinguish between the different known quantum phases. Importantly, this is achieved in a fully unsupervised manner, with the model autonomously discovering latent factors that correspond to physically meaningful degrees of freedom.

Looking ahead, we note that in this study we restricted our analysis to spin models with a sign-positive ground state, so that measurement snapshots from a single computational basis sufficed. A natural next step is to lift this constraint and address systems with non-positive ground state, where faithful reconstruction will demand data drawn from several complementary measurement bases to capture the full quantum structure. Likewise, although our benchmarks focused on interacting two-level systems— $S = 1/2$ spins and Rydberg atoms—the underlying methodology is readily transferrable to a broader class of platforms. With suitable decoder designs that reflect the statistics of the target system, the same prior-aligned VAE framework could be deployed to quantum circuits, d -level and/or multi-species.

The proposed framework can also be integrated with complementary interpretable techniques. For instance, equipping the encoder with correlator neural networks—architectures designed to capture designated local and non-local correlations in the data [11]—would allow the latent variables to be analysed in tandem with explicit correlation features, yielding a richer, more transparent description of the underlying physics. Furthermore, as demonstrated in Section III A, symbolic-regression methods offer a promising approach to extracting compact analytical expressions from the learned latents. The dimensionality and structure revealed by the cpVAE can in turn serve as informed priors for such regression algorithms, accelerating their convergence and enhancing the interpretability of the resulting formulae.

V. ACKNOWLEDGMENTS

We sincerely thank Hannes Pichler, Sepehr Ebadi, Tout Wang, and Mikhail Lukin for providing the experimental data on the Rydberg atoms.

This research was funded in part by the Austrian Science Fund (FWF) [SFB BeyondC F7102, 10.55776/F71]. For open access purposes, the author has applied a CC BY public copyright license to any author accepted manuscript version arising from this submission. This work was also supported by the European Union (ERC Advanced Grant, QuantAI, No. 101055129). The views and opinions expressed in this article are however those of the author(s) only and do not necessarily reflect those of the European Union or the European Research Council - neither the European Union nor the granting authority

can be held responsible for them. This research used resources of the National Energy Research Scientific Computing Center (NERSC), a Department of Energy User Facility using NERSC award ERCAP0032002.

VI. CODE AVAILABILITY

The code needed to reproduce the results presented in this work is available in Ref. [29]. The datasets for the NNN-TFIM and the LR-TFIM were created by means of NetKet [38, 39], which is based on Jax [40] and MPI4Jax [41]. Netket has also been used for implementing the dense ARNN used as decoder of the cpVAE on the spin models. The implementation of the TC loss (Eq. (7)) was done based on the implementation in [42]. The neural networks have been implemented using Flax [43].

-
- [1] R. Iten, T. Metger, H. Wilming, L. del Rio, and R. Renner, Discovering physical concepts with neural networks, *Phys. Rev. Lett.* **124**, 010508 (2020).
 - [2] J. Carrasquilla and R. G. Melko, Machine learning phases of matter, *Nature Physics* **13**, 431.
 - [3] K. Cybiński, J. Enouen, A. Georges, and A. Dawid, *Speak so a physicist can understand you! tetriscnn for detecting phase transitions and order parameters* (2024), arXiv:2411.02237 [quant-ph].
 - [4] C. Miles, R. Samajdar, S. Ebadi, T. T. Wang, H. Pichler, S. Sachdev, M. D. Lukin, M. Greiner, K. Q. Weinberger, and E.-A. Kim, Machine learning discovery of new phases in programmable quantum simulator snapshots, *Phys. Rev. Res.* **5**, 013026 (2023).
 - [5] L. Mauron, Z. Denis, J. Nys, and G. Carleo, *Predicting topological entanglement entropy in a rydberg analog simulator* (2024), arXiv:2406.19872 [quant-ph].
 - [6] G. Torlai, G. Mazzola, J. Carrasquilla, M. Troyer, R. Melko, and G. Carleo, Neural-network quantum state tomography, *Nature Physics* **14**, 447.
 - [7] G. Carleo and M. Troyer, Solving the quantum many-body problem with artificial neural networks, *Science* **355**, 602 (2017), <https://www.science.org/doi/pdf/10.1126/science.aag2302>.
 - [8] S. J. Wetzel, S. Ha, R. Iten, M. Kłopotek, and Z. Liu, *Interpretable machine learning in physics: A review* (2025), arXiv:2503.23616 [physics.comp-ph].
 - [9] P. Ponte and R. G. Melko, Kernel methods for interpretable machine learning of order parameters, *Physical Review B* **96**, 205146 (2017).
 - [10] Y. Kharkov, O. Shtanko, A. Seif, P. Bienias, M. Van Regemortel, M. Hafezi, and A. V. Gorshkov, Discovering hydrodynamic equations of many-body quantum systems, arXiv preprint arXiv:2111.02385 (2021).
 - [11] C. Miles, A. Bohrdt, R. Wu, C. Chiu, M. Xu, G. Ji, M. Greiner, K. Q. Weinberger, E. Demler, and E.-A. Kim, Correlator convolutional neural networks as an interpretable architecture for image-like quantum matter data, *Nature Communications* **12**, 3905 (2021).
 - [12] D. P. Kingma, M. Welling, *et al.*, Auto-encoding variational bayes (2013).
 - [13] I. Higgins, L. Matthey, A. Pal, C. Burgess, X. Glorot, M. Botvinick, S. Mohamed, and A. Lerchner, beta-VAE: Learning basic visual concepts with a constrained variational framework, in *International Conference on Learning Representations* (2017).
 - [14] N. Walker, K.-M. Tam, and M. Jarrell, Deep learning on the 2-dimensional ising model to extract the crossover region with a variational autoencoder, *Scientific Reports* **10**, 13047.
 - [15] A. Naravane and N. Mathur, *Semi-supervised learning of order parameter in 2d ising and xy models using conditional variational autoencoders* (2023), arXiv:2306.16822 [cond-mat.stat-mech].
 - [16] S. Ebadi, T. T. Wang, H. Levine, A. Keesling, G. Semeghini, A. Omran, D. Bluvstein, R. Samajdar, H. Pichler, W. W. Ho, S. Choi, S. Sachdev, M. Greiner, V. Vuletić, and M. D. Lukin, Quantum phases of matter on a 256-atom programmable quantum simulator, *Nature* **595**, 227.
 - [17] B.-W. Li, Y.-K. Wu, Q.-X. Mei, R. Yao, W.-Q. Lian, M.-L. Cai, Y. Wang, B.-X. Qi, L. Yao, L. He, Z.-C. Zhou, and L.-M. Duan, Probing critical behavior of long-range transverse-field ising model through quantum kibble-zurek mechanism, *PRX Quantum* **4**, 010302 (2023).
 - [18] Z. Patel, E. Merali, and S. J. Wetzel, Unsupervised learning of rydberg atom array phase diagram with siamese neural networks, *New Journal of Physics* **24**, 113021 (2022).
 - [19] A. Suresh, H. Schlömer, B. Hashemi, and A. Bohrdt, Interpretable correlator Transformer for image-like quantum matter data, *arXiv e-prints*, arXiv:2407.21502 (2024), arXiv:2407.21502 [cond-mat.quant-gas].
 - [20] S. J. Wetzel, Unsupervised learning of phase transitions: From principal component analysis to variational autoencoders, *Phys. Rev. E* **96**, 022140 (2017).
 - [21] I. Jang and A. Yethiraj, Unsupervised machine learning method for the phase behavior of the constant magnetization ising model in two and three dimensions, *The Journal of Physical Chemistry B* **129**, 532.
 - [22] F. Frohnert and E. van Nieuwenburg, Explainable representation learning of small quantum states, *Machine Learning: Science and Technology* **5**, 015001 (2024).

- [23] H. Poulsen Nautrup, T. Metger, R. Iten, S. Jerbi, L. M. Trenkwalder, H. Wilming, H. J. Briegel, and R. Renner, Operationally meaningful representations of physical systems in neural networks, *Machine Learning: Science and Technology* **3**, 045025 (2022).
- [24] G. Fernández-Fernández, C. Manzo, M. Lewenstein, A. Dauphin, and G. Muñoz Gil, Learning minimal representations of stochastic processes with variational autoencoders, *Phys. Rev. E* **110**, L012102 (2024).
- [25] J. Arnold, F. Schäfer, A. Edelman, and C. Bruder, Mapping out phase diagrams with generative classifiers, *Phys. Rev. Lett.* **132**, 207301 (2024).
- [26] H. Lange, A. Van de Walle, A. Abedinnia, and A. Bohrdt, From architectures to applications: a review of neural quantum states, *Quantum Science and Technology* **9**, 040501 (2024).
- [27] A. Chen, V. D. Naik, and M. Heyl, *Convolutional transformer wave functions* (2025), arXiv:2503.10462 [cond-mat.dis-nn].
- [28] R. T. Q. Chen, X. Li, R. B. Grosse, and D. K. Duvenaud, Isolating sources of disentanglement in variational autoencoders, in *Advances in Neural Information Processing Systems*, Vol. 31, edited by S. Bengio, H. Wallach, H. Larochelle, K. Grauman, N. Cesa-Bianchi, and R. Garnett (Curran Associates, Inc., 2018).
- [29] H. P. N. Paulin de Schouepnikoff, Gorka Muñoz-Gil and H. J. Briegel, *Code Repository - Representation learning of quantum data with probabilistic VAEs* (2025).
- [30] F. A. Kassan-ogly, One-dimensional ising model with next-nearest-neighbour interaction in magnetic field, *Phase Transitions: A Multinational Journal* **74**, 353 (2001).
- [31] P. Hauke and L. Tagliacozzo, Spread of correlations in long-range interacting quantum systems, *Phys. Rev. Lett.* **111**, 207202 (2013).
- [32] P. Jurcevic, B. P. Lanyon, P. Hauke, C. Hempel, P. Zoller, R. Blatt, and C. F. Roos, Quasiparticle engineering and entanglement propagation in a quantum many-body system, *Nature* **511**, 202.
- [33] M. Cranmer, *Interpretable machine learning for science with pysr and symbolicregression.jl* (2023), arXiv:2305.01582 [astro-ph.IM].
- [34] M. L. Baez, M. Goihl, J. Haferkamp, J. Bermejo-Vega, M. Gluza, and J. Eisert, Dynamical structure factors of dynamical quantum simulators, *Proceedings of the National Academy of Sciences* **117**, 26123 (2020).
- [35] D. Vodola, L. Lepori, E. Ercolessi, and G. Pupillo, Long-range ising and kitaev models: phases, correlations and edge modes, *New Journal of Physics* **18**, 015001 (2015).
- [36] M. D. Lukin, M. Fleischhauer, R. Cote, L. Duan, D. Jaksch, J. I. Cirac, and P. Zoller, Dipole blockade and quantum information processing in mesoscopic atomic ensembles, *Physical review letters* **87**, 037901 (2001).
- [37] E. Urban, T. A. Johnson, T. Henage, L. Isenhower, D. Yavuz, T. Walker, and M. Saffman, Observation of rydberg blockade between two atoms, *Nature Physics* **5**, 110 (2009).
- [38] F. Vicentini, D. Hofmann, A. Szabó, D. Wu, C. Roth, C. Giuliani, G. Pescia, J. Nys, V. Vargas-Calderón, N. Astrakhantsev, and G. Carleo, NetKet 3: Machine Learning Toolbox for Many-Body Quantum Systems, *SciPost Phys. Codebases* , 7 (2022).
- [39] F. Vicentini, D. Hofmann, A. Szabó, D. Wu, C. Roth, C. Giuliani, G. Pescia, J. Nys, V. Vargas-Calderón, N. Astrakhantsev, and G. Carleo, Codebase release 3.4 for NetKet, *SciPost Phys. Codebases* , 7 (2022).
- [40] J. Bradbury, R. Frostig, P. Hawkins, M. J. Johnson, C. Leary, D. Maclaurin, G. Necula, A. Paszke, J. VanderPlas, S. Wanderman-Milne, and Q. Zhang, *JAX: composable transformations of Python+NumPy programs* (2018).
- [41] H. Dion and V. Filippo, mpi4jax: Zero-copy mpi communication of jax arrays, *Journal of Open Source Software* **6**, 3419 (2021).
- [42] Y. Dubois, A. Kastanos, D. Lines, and B. Melman, Disentangling vae, <http://github.com/YannDubs/disentangling-vae/> (2019).
- [43] J. Heek, A. Levskaya, A. Oliver, M. Ritter, B. Rondepierre, A. Steiner, and M. van Zee, *Flax: A neural network library and ecosystem for JAX* (2024).
- [44] A. Vaswani, N. Shazeer, N. Parmar, J. Uszkoreit, L. Jones, A. N. Gomez, L. u. Kaiser, and I. Polosukhin, Attention is all you need, in *Advances in Neural Information Processing Systems*, Vol. 30, edited by I. Guyon, U. V. Luxburg, S. Bengio, H. Wallach, R. Fergus, S. Vishwanathan, and R. Garnett (Curran Associates, Inc., 2017).
- [45] G. Klambauer, T. Unterthiner, A. Mayr, and S. Hochreiter, Self-normalizing neural networks, in *Advances in Neural Information Processing Systems*, Vol. 30, edited by I. Guyon, U. V. Luxburg, S. Bengio, H. Wallach, R. Fergus, S. Vishwanathan, and R. Garnett (Curran Associates, Inc., 2017).
- [46] D. Fitzek, Y. H. Teoh, H. P. Fung, G. A. Dagnew, E. Merali, M. S. Moss, B. MacLellan, and R. G. Melko, *Rydberggpt* (2024), arXiv:2405.21052 [quant-ph].
- [47] J. Zhuang, T. Tang, Y. Ding, S. C. Tatikonda, N. Dvornek, X. Papademetris, and J. Duncan, Adabelief optimizer: Adapting stepsizes by the belief in observed gradients, in *Advances in Neural Information Processing Systems*, Vol. 33, edited by H. Larochelle, M. Ranzato, R. Hadsell, M. Balcan, and H. Lin (Curran Associates, Inc., 2020) pp. 18795–18806.
- [48] L. N. Smith, *A disciplined approach to neural network hyper-parameters: Part 1 – learning rate, batch size, momentum, and weight decay* (2018), arXiv:1803.09820 [cs.LG].
- [49] Y. Li, T. Kind, J. Folz, A. Vaniya, S. S. Mehta, and O. Fiehn, Spectral entropy outperforms MS/MS dot product similarity for small-molecule compound identification, *Nature Methods* **18**, 1524.
- [50] P.-Y. Xiong, H. Jahanshahi, R. Alcaraz, Y.-M. Chu, J. F. Gómez-Aguilar, and F. E. Alsaadi, Spectral entropy analysis and synchronization of a multi-stable fractional-order chaotic system using a novel neural network-based chattering-free sliding mode technique, *Chaos, Solitons & Fractals* **144**, 110576.
- [51] A. Swetapadma, T. Shuvam, and N. Behera, A novel fault identification technique for transmission lines based on spectral entropy and one-dimensional cnn, in *2023 Fifth International Conference on Electrical, Computer and Communication Technologies (ICECCT)* (2023) pp. 01–05.

Appendix A: Neural network architectures

In this section, we provide further details on the architecture of the neural network used for the encoder and decoder of the dVAE and the cpVAE through the different scenarios presented in the main text.

1. Encoder

For the VAEs trained on both spin models in Section III A, a convolutional neural network was used as the encoder. The details of its architecture are presented in Table I. The same architecture is used for both dVAE and cpVAE.

Layer type	Output size
Input	$B \times N \times 1$
Circular Conv 1D ($k_s = 3$)	$B \times N \times 32$
relu	$B \times N \times 32$
Circular Conv 1D ($k_s = 3$)	$B \times N \times 32$
relu	$B \times N \times 32$
Global Average Pooling	$B \times 32$
Mean predictions:	
Dense	$B \times 64$
relu	$B \times 64$
Dense	$B \times 5$
Variance predictions:	
Dense	$B \times 64$
relu	$B \times 64$
Dense	$B \times 5$

TABLE I. **Convolutional encoder.** Details on the encoder architecture used for the NNN-TFIM and the LR-TFIM. B is the batch size, N the size of the spin configurations and k_s the kernel size. The latent space dimension was chosen to be 5. The same architecture is used for the dVAE and the cpVAE.

On the other hand, for the cpVAE trained on snapshots of Rydberg atom arrays (Section III B), we used a transformer architecture for its encoder [44]. Further details are presented in Table II.

Layer type	Output size
Input	$B \times N \times 1$
Embedding	$B \times N \times d_{\text{model}}$
Positional Encoding (sin)	$B \times N \times d_{\text{model}}$
Transformer layer (3x):	
Normalization	$B \times N \times d_{\text{model}}$
Self-Attention ($N_{\text{head}} = d_{\text{model}}/2$)	$B \times N \times d_{\text{model}}$
Residual Connection	$B \times N \times d_{\text{model}}$
Dense	$B \times 4 \cdot d_{\text{model}}$
relu	$B \times d_{\text{model}}$
Dense	$B \times N \times d_{\text{model}}$
Residual Connection	$B \times N \times d_{\text{model}}$
Normalization	$B \times N \times d_{\text{model}}$
Mean predictions:	
Dense	$B \times d_{\text{latent}}$
Variance predictions:	
Dense	$B \times d_{\text{latent}}$

TABLE II. **Transformer encoder.** Details on the encoder architecture used for the cpVAE trained on snapshots of Rydberg atoms. B is the batch size, N is the number of atoms. A dimension of $d_{\text{model}} = 8$ was used. The latent space dimension was chosen to be 5.

2. Autoregressive decoder

As mentioned in the main text (see Section II), autoregressive neural network are used to model the conditional probabilities of each spin values

$$p_\theta(x) = \prod_i p_\theta(x_i | x_0, x_1, \dots, x_{i-1}). \quad (\text{A1})$$

Each conditional $p_\theta(x_i | x_0, \dots, x_{i-1})$ being normalized, this allow to sample spin configuration directly, without any Markov chain, typically needed for non-autoregressive models.

A common approach to render a neural network autoregressive is to impose a masking scheme that prevents access to future elements of the input sequence. For models trained on spin models (Section III A), we use as the decoder of the cpVAE a standard feedforward neural network (FFNN), with the masking being achieved by simply imposing triangular weights. For the numerical simulations, we use 3 hidden layers with 80 hidden neurons and *selu* activation functions [45]. This design choice allowed us to employ the same neural network architecture for the decoder of the dVAE, omitting only the autoregressive masking used in the cpVAE. This ensures that comparisons between the two models remain as fair as possible.

For the Rydberg atom arrays, as inspired by Ref. [46], we use the typical transformer architecture [44] for the decoder of the cpVAE, as detailed in Table III. The latent representation output by the encoder is fed into the transformer as context, following the typical context-based attention mechanism.

Layer type	Output size
Input	$B \times N \times 1$
Embedding	$B \times N \times d_{\text{model}}$
Positional Encoding (sin)	$B \times N \times d_{\text{model}}$
Shift	$B \times N \times d_{\text{model}}$
Transformer layer (3x):	
Normalization	$B \times N \times d_{\text{model}}$
Causal Self-Attention ($N_{\text{head}} = d_{\text{model}}/2$)	$B \times N \times d_{\text{model}}$
Context Based Attention ($N_{\text{head}} = d_{\text{model}}/2$)	$B \times N \times d_{\text{model}}$
Residual Connection	$B \times N \times d_{\text{model}}$
Dense	$B \times 4 \cdot d_{\text{model}}$
relu	$B \times d_{\text{model}}$
Dense	$B \times N \times d_{\text{model}}$
Residual Connection	$B \times N \times d_{\text{model}}$
Normalization	$B \times N \times d_{\text{model}}$
Dense	$B \times N \times 2$
Log softmax	$B \times N \times 2$

TABLE III. **Transformer decoder.** Details on the decoder architecture used for cpVAE trained on snapshots of the Rydberg atoms. B is the batch size and N the number of atoms. For the model presented in the main text, we fixed $d_{\text{model}} = 8$ and the latent space dimension to $d_{\text{latent}} = 5$. Not shown here, the context vector used in the context-based attention are the latent variables z_i , after a linear layer expending their dimension to $B \times d_{\text{latent}} \times d_{\text{model}}$

Appendix B: Training details

1. Training hyperparameters

In this section, we present the hyperparameters used for the numerical simulations. In particular, we will present the details on the training sets, the strength of each term in the loss (see Eq. (7)) and the optimizer used for the gradient descent.

For both spin models, datasets were generated by sampling 10^4 spin configurations from the exact ground state wavefunctions, computed using the Lanczos algorithm. For the NNN-TFIM, the Hamiltonian parameters (J_2, h) (see Eq. (8)) were varied over a regular grid of (21, 41) values. The coupling J_2 was linearly spaced in the interval $[0, 1]$, while the transverse field h was linearly spaced in $[0, 2]$. For the LR-TFIM (see Eq. (9)), the exponent α and transverse field h were varied over a (20, 20) grid. The values of α were linearly spaced in $[1, 5]$, whereas h was logarithmically spaced in the range $[1.6, 10]$.

For the experimental system of Rydberg atoms, we had access to 250 snapshots taken for each set of parameters $(R_b/a, \Delta/\Omega)$. In particular, the parameters were

$$R_b/a \in \{1.01, 1.05, 1.13, 1.23, 1.3, 1.39, 1.46, 1.56, 1.65, 1.71, 1.81, 1.89, 1.97\} \quad (\text{B1})$$

and 31 values of $\Delta/\Omega \in [-2.33, 4.65]$, linearly spaced.

The values used for the hyperparameters in the TC regularization (see Eq. (7)) are presented in Table IV. A linear schedule was used for the weight on the component-wise KL, from γ_{min} to γ_{max} .

Spin model	α	β	γ_{min}	γ_{max}
NNN-TFIM	0.1	30	0.1	0.2
LR-TFIM	0.1	0.5	0.5	10
Rydberg	0.001	10	1	1

TABLE IV. **TC regularization hyperparameters** Values of the hyperparameters used in Eq. (7) for training the cpVAE on the two spin models and on the Rydberg atom arrays snapshots.

We then optimized the neural network with the *adabelief* optimizer [47], with default parameters and a learning rate of 0.001.

2. Training curves

In this section, we provide additional details on the training of the dVAE and the cpVAE. The training dynamics of both VAEs on the NNN-TFIM and LR-TFIM are presented in Fig. 5 and Fig. 6, respectively. We show the evolution of the reconstruction loss $\mathcal{L}_{reconstr.}$ and the logarithm of the latent variances $\log \sigma_i$ output by the encoder.

For the dVAE, the reconstruction loss corresponds to the mean squared error (MSE). Across both spin models, this loss decreases rapidly in the early training stages and subsequently plateaus. This typically indicates that the model has insufficient capacity or expressivity to fully learn the data distribution [48]. In our case, as shown in the main text, this model was not able to approximate the quantum probability distribution and capture the correlations. As discussed in the main text, in order to ensure a fair comparison between the dVAE and cpVAE, the dVAE was trained without KL regularization. Additionally, its latent dimension was fixed to match the expected number of relevant latent factors, as found by the cpVAE and previously known for the presented benchmark cases. Under these conditions, we observe that the variances $\log \sigma_i$ decrease rapidly for both spin models (see more about this below).

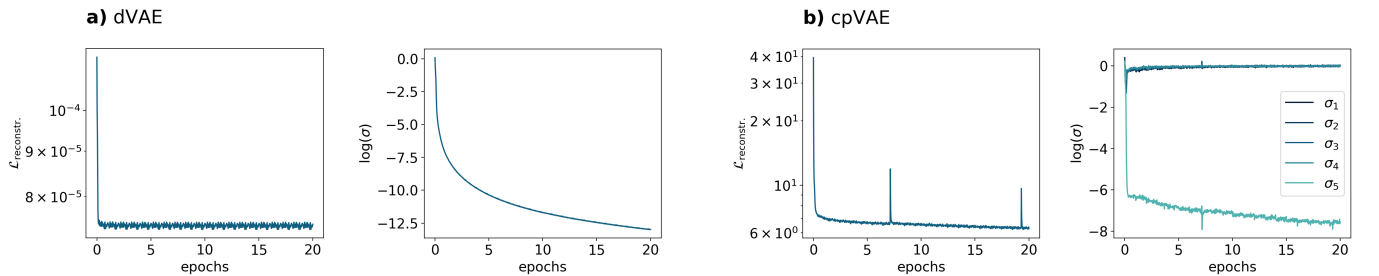


FIG. 5. **Training: NNN-TFIM.** Training of a) the dVAE and b) the cpVAE seen through the reconstruction loss $\mathcal{L}_{reconstr.}$ and the log of the variances σ_i output by the encoder. For the dVAE the reconstruction loss is the mean square error (MSE) and for the cpVAE it is the first term in Eq. (7).

For the cpVAE, the reconstruction loss corresponds to the first term in Eq. (7). During training, this loss exhibits a rapid initial decrease followed by a more gradual decline, accompanied by small fluctuations characteristic of stochastic mini-batch optimization. The evolution of the logarithmic variances $\log \sigma_i$ for the five latent neurons is also displayed. In the case of the NNN-TFIM, the model selectively activates a single latent neuron, indicated by a decrease in its $\log \sigma_i$, while effectively suppressing the remaining neurons by driving their variances close to zero. This behavior reflects a sparsity in the learned latent representation, consistent with the existence of a dominant underlying feature in the data. For the LR-TFIM, the model retains two active latent neurons. Notably, the activation of the second latent neuron occurs after approximately one epoch of training, enabling the model to further reduce the reconstruction loss. This dynamic reflects the model's ability to progressively allocate capacity as needed to capture increasingly complex structure in the data.

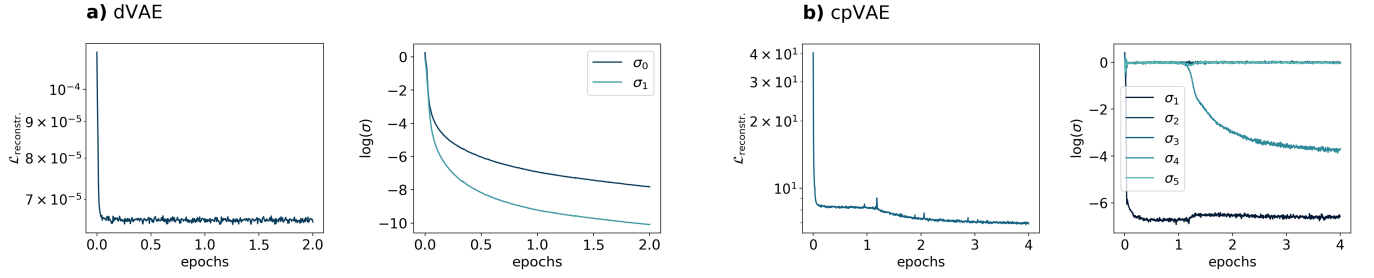


FIG. 6. **Training: LR-TFIM.** Training of a) the dVAE and b) the cpVAE seen through the reconstruction loss $\mathcal{L}_{\text{reconstr.}}$ and the log of the variances σ_i output by the encoder. For the dVAE the reconstruction loss is the mean square error (MSE) and for the cpVAE it is the first term in Eq. (7).

Finally, we present the training dynamics of the cpVAE on experimental snapshots of Rydberg atoms in Fig. 7. The reconstruction loss decreases smoothly over time, and the model rapidly converges to a representation involving two active latent neurons, as evidenced by the corresponding drop in $\log \sigma_{1,5}$. The remaining neurons are effectively noised out by pushing their variances near zero, again indicating a sparse and interpretable latent encoding.

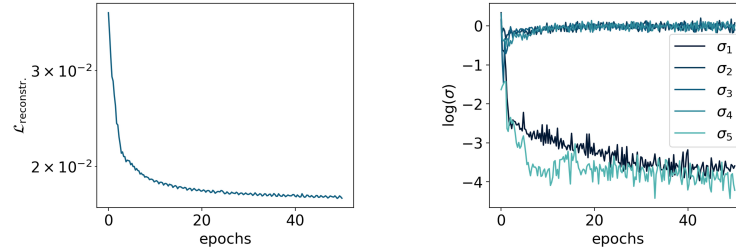


FIG. 7. **Training: Rydberg atoms.** Training of the cpVAE seen through the reconstruction loss $\mathcal{L}_{\text{reconstr.}}$ (left) and the log of the variances σ_i output by the encoder (right).

Appendix C: NNN-TFIM: Generalization abilities

The generalization capabilities of the dVAE and cpVAE were also investigated on the NNN-TFIM using a restricted training set. Specifically, both models were trained without any spin configuration coming from the region $0.4 < h < 0.75$ of the parameter space. We then evaluated the generation performance of both models across the entire phase space, including the excluded region. The reconstructed values of the nearest-neighbor correlator are presented in Fig. 8a) and b) for the dVAE and cpVAE, respectively. Notably, the quality of the reconstructed correlators in the previously unseen region remains consistent with that of the training regions. This indicates that both architectures exhibit robust generalization to regions of the phase space that were not included in the training set.

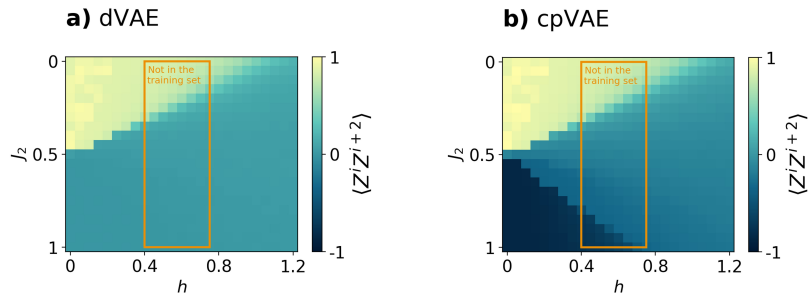


FIG. 8. **Generalization abilities: NNN-TFIM.** Next-nearest-neighbour correlator of the spin configuration generated by a) the dVAE and b) the cpVAE. The training of both VAE were performed without spin configurations coming from the ground state of Hamiltonians having $0.4 < h < 0.75$, region inside the orange rectangle. Then they are tested on the entire space.

Appendix D: LR-TFIM: Sampling from the latent space

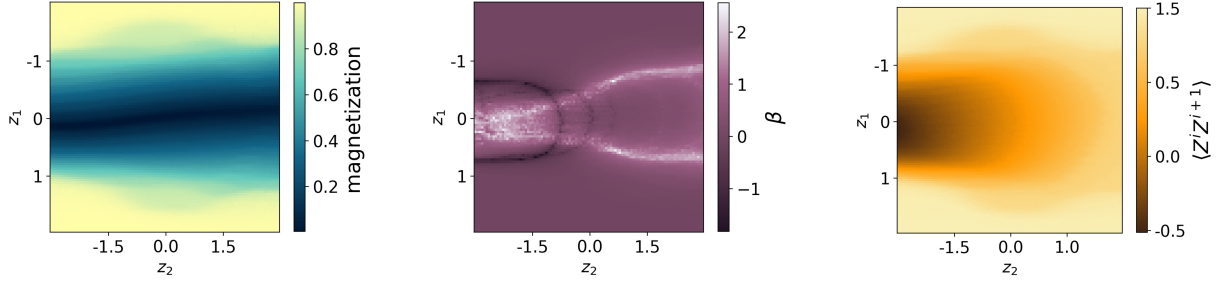


FIG. 9. **Generation: LR-TFIM.** To further interpret the structure learned by the cpVAE, a scan is performed over the latent variables $z_{1,2}$. Then, for each values of the latter, samples are generated using the decoder of the cpVAE. Left is the magnetization of these samples, middle is the β exponent and right is the correlators $\langle Z^i Z^{i+1} \rangle$.

To further interpret the structure learned by the cpVAE, we leverage its generative nature to probe the contents of the latent space. A linear sweep is performed over each latent dimension independently, and for every point along the scan, 1000 spin configurations are sampled from the generative decoder. For each set of generated configurations, we compute the magnetization, the correlation exponent β and the nearest neighbour correlator $\langle Z^i Z^{i+1} \rangle$. The results are presented in Fig. 9. This generative probing again highlights that the two latent dimensions encode distinct physical features: the first latent neuron predominantly controls the magnetization of the output configurations, while the second mainly governs their correlation. Notably, for certain latent values, the model generates spin configurations with an apparent $\beta < 0$. These correspond to atypical states that exhibit very weak or inverted correlation patterns, in which nearest-neighbour correlations vanish and increase slightly with distance. In these cases, the power-law fit used to estimate β becomes unreliable.

Appendix E: Study of the latent neuron variances for spin models benchmarks

In the main text, we discuss the behavior of the latent variances σ_i output by the cpVAE encoder when trained on Rydberg atom snapshots (see Section III B). Here we present an extended analysis of the variances output by the encoder of the cpVAE trained on the spin models (see Section III A).

As commented in the main text, the variances output by the encoder reflect the permissible level of noise in the sampling of the latent variables z_i such that the decoder can still accurately reconstruct the input. Empirically, we observe that these variances tend to correlate with the degree of apparent randomness in the input data. To quantify this relationship, we compare the learned variances with the spectral entropy of the input spin configurations. Spectral entropy is a scalar metric that captures the randomness or complexity of a signal, and is particularly well-suited for binary data such as spin configurations. The core idea is that structured signals concentrate their spectral power in specific frequency components, whereas random signals exhibit a more uniform distribution across the frequency domain. Consequently, the spectral entropy serves as a compact and informative measure of the underlying order or disorder in the input data.

From a practical perspective, the spectral entropy compresses the normalized power spectral density of a signal into a single scalar value, and is computed using the Shannon entropy of its frequency distribution. In this framework, lower spectral entropy corresponds to more structured, periodic, input configurations, while higher values indicate increased stochasticity and disorder. This metric has been employed across various domains, including molecular component identification [49], the characterization of chaotic dynamics [50] and classification tasks [51], demonstrating its broad applicability for quantifying structure and randomness in complex data.

To compute such metric, we begin by applying a fast Fourier transform (FFT) to the spin configuration. The power spectrum is then obtained by taking the squared magnitude of the FFT coefficients. This spectrum is normalized such that it can be interpreted as a probability distribution I_p , from which the Shannon entropy S is calculated as

$$S = - \sum_p I_p \log I_p. \quad (\text{E1})$$

The values of σ_i output by the encoder of the cpVAE are shown in Fig. 10 as a function of the spectral entropy of the input spin configuration. Overall, a linear dependence between their logarithm $\log \sigma_i$ and the spectral entropy is observed.

This trend can be understood through the competing objectives of the VAE’s loss function Eq. (1): the reconstruction term $\mathcal{L}_{\text{reconstruction}}$ versus the Kullback–Leibler regularization term \mathcal{L}_{KL} . When the input exhibits a high degree of regularity and is easier to predict, the encoder can output smaller $|\log \sigma_i|$ values, thereby reducing the KL contribution to the total loss. Conversely, inputs with higher spectral entropy—indicative of greater randomness—necessitate larger encoder variances to preserve sufficient flexibility in the latent representation for accurate reconstruction.

Notably, for the NNN-TFIM, this relationship exhibits a piecewise linear or ”two-regime” behavior. Specifically, spin configurations from the antiferromagnetic phase require systematically higher latent variances compared to those from the ferromagnetic phase, even when their spectral entropy values are comparable. This observation suggests that the antiferromagnetic phase encodes richer, more intricate structure, requiring the model to allocate greater representational capacity to faithfully encode these configurations.

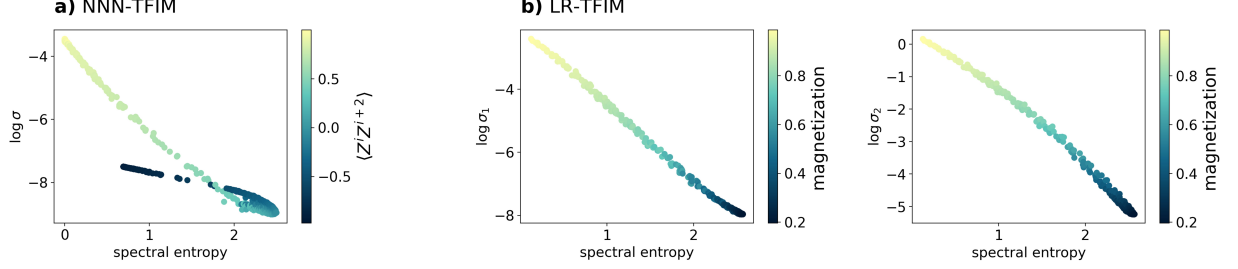


FIG. 10. **Behavior of the latent variances σ for the NNN-TFIM and the LR-TFIM.** We show here the output σ_i of the cpVAE encoder as a function of the spectral entropy of the input spin configurations. **a)** NNN-TFIM, where a single latent neuron remains active after training. **b)** LR-TFIM, for which two latent neurons remained active.